

Anisotropic Diffusion in a Toroidal Geometry

Paul F. Fischer

Mathematics and Computer Science Division, Argonne National Laboratory, Argonne, IL 60439, U.S.A.

E-mail: fischer@mcs.anl.gov

Abstract. As part of the Department of Energy’s applications oriented SciDAC project, three model problems have been proposed by the Center for Extended Magnetohydrodynamics Modeling to test the potential of numerical algorithms for challenging magnetohydrodynamics (MHD) problems that are required for future fusion development. The first of these, anisotropic diffusion in a toroidal geometry, is considered in this note.

1. Introduction

Three model problems have been proposed by the Center for Extended Magnetohydrodynamics Modeling (CEMM) to test the potential of numerical algorithms for the challenging MHD problems required for further development of fusion technology. The first of these is the problem of anisotropic diffusion in a toroidal geometry. This report presents implementation details and results for application of the spectral element (SE) method to the anisotropic diffusion problem. Similar analyses of high-order performance have recently been reported in [4, 5]. The focus here is primarily on the error behavior as a function of the SE discretization parameters. No attempt has been made to adaptively refine the mesh nor to optimize the preconditioners for this class of problems. We discuss the potential of such enhancements in our closing remarks.

2. Anisotropic Diffusion

We consider the unsteady diffusion problem

$$\frac{\partial u}{\partial t} - \nabla \cdot \mathbf{K} \cdot \nabla u = f \quad \text{in } \Omega, \quad (1)$$

where Ω is the toroidal geometry illustrated in Fig. 1(a). The major radius of the torus is R_0 , and the minor radius is a . The temperature, u , satisfies homogeneous Dirichlet boundary conditions on the boundary $\partial\Omega$. The conductivity, $\mathbf{K} = \kappa_{\parallel} \tilde{\mathbf{K}} + \kappa_I \mathcal{I}$, is a 3 by 3 tensor comprising two parts. The first part is the parallel conductivity given by $\kappa_{\parallel} \tilde{\mathbf{K}} := \kappa_{\parallel} \mathbf{b} \mathbf{b}^T / |\mathbf{b}|^2$, where κ_{\parallel} is the parallel diffusion coefficient and \mathbf{b} is a prescribed magnetic vector-field. The second component, $\kappa_I \mathcal{I}$, is the standard isotropic diffusion term, with \mathcal{I} the 3 by 3 identity tensor. Generally, the diffusion is strongly anisotropic, with $\kappa_{\parallel} \gg \kappa_I$, which implies that diffusion along the torus axis is much more rapid than across the torus cross-section. Typical anisotropy ratios are $\kappa_{\parallel} / \kappa_I \simeq 10^9$.

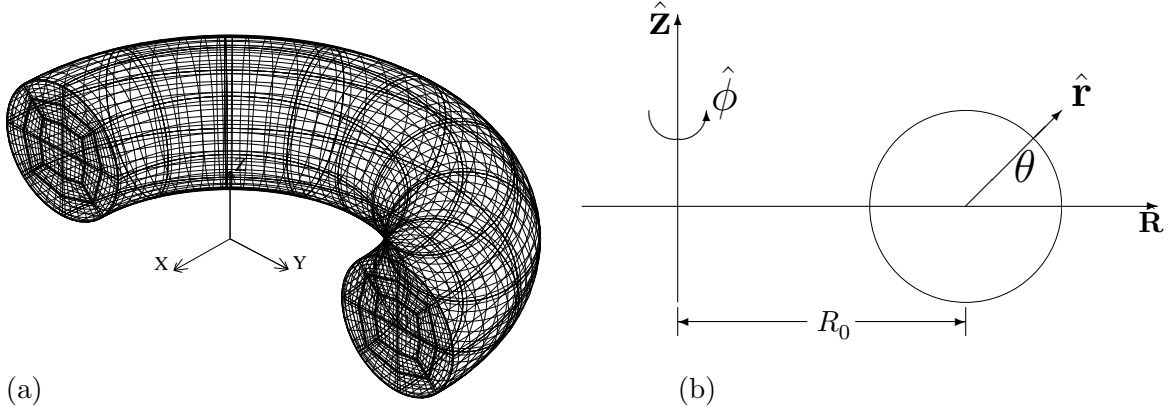


Figure 1. (a) Cut-away view of a 20×32 $[(\hat{\mathbf{r}}, \hat{\theta}) \times \hat{\phi}]$ spectral element mesh. The finely spaced grid lines indicate the tensor-product GLL mesh for $N = 7$. (b) Toroidal coordinate system.

The prescribed magnetic field, $\mathbf{b} = \mathbf{b}_0 + \nabla \times \alpha \mathbf{b}_0$, consists of an axisymmetric base field,

$$\mathbf{b}_0 := -\nabla \times \left(\frac{\psi}{R} \hat{\phi} \right) + \frac{1}{R} \hat{\phi} = \frac{1}{R} \left(\frac{\partial \psi}{\partial z} \hat{\mathbf{R}} + \hat{\phi} - \frac{\partial \psi}{\partial R} \hat{\mathbf{z}} \right),$$

plus a sinusoidal perturbation, $\nabla \times \alpha \mathbf{b}_0$. The functions ψ and α are [6]

$$\psi(R, z) := C_\psi \ln \left[1 + \frac{r^2}{a^2} \right], \quad \alpha := C_\alpha \sin(m\theta - n\phi) g(r), \quad (2)$$

with constants

$$C_\psi := \frac{a^2}{2R_0 q_0}, \quad C_\alpha := \frac{\alpha_{mn} a^2}{8R_0 q_0}. \quad (3)$$

Here, θ and r represent polar coordinates with origin at $R = R_0$, $z = 0$, as illustrated in Fig. 1(b); the perturbation wavenumbers m and n are integers; α_{mn} is the perturbation amplitude; and $g(r)$ is an order unity damping function that scales as r^m at $r = 0$ and vanishes at $r = a_0$.

In the (r, θ, ϕ) coordinate system, the base field is

$$\mathbf{b}_0 = \frac{1}{R} \left(\hat{\phi} - C_\psi \frac{2r}{a^2 + r^2} \hat{\theta} \right) \quad (4)$$

and thus comprises field lines that are helically wrapped on toroidal (constant r) surfaces. In the following, we take $R_0 = 3$ and $a=1$, which implies that there is a 3–2 rational surface at $r = r_* \approx .6790229$ on which the base field lines wrap back upon themselves after two turns in θ and three turns in ϕ . We will consider the interaction of this rational surface with the $(m, n) = (3, 2)$ perturbation mode in Section 6.

3. Spectral Element Discretization

The spectral element discretization of (1) is based on the weighted residual formulation: Find $u \in \mathcal{H}_0^1(\Omega)$ such that

$$\frac{d}{dt} \int_{\Omega} v u d\mathbf{x} - \int_{\Omega} (\nabla v) \cdot \mathbf{K} \cdot (\nabla u) d\mathbf{x} = \int_{\Omega} v f d\mathbf{x} \quad \forall v \in \mathcal{H}_0^1(\Omega), \quad (5)$$

where $\mathcal{H}_0^1(\Omega)$ is the usual Sobolev space of functions belonging to L^2 whose derivatives also belong to L^2 . The essential features of the variational formulation are that it reduces the continuity requirements on u from C^1 to C^0 and that it guarantees a symmetric positive definite (SPD) linear system for the stiffness matrix (provided that \mathbf{K} is SPD). Discretization by finite or spectral elements amounts to restricting the search and trial spaces (for u and v , respectively) to a finite-dimensional subspace $X^N \subset \mathcal{H}_0^1$, choosing a bases for this space, and solving for the basis coefficients such that (5) is satisfied. For a Galerkin formulation, one employs the same space and basis for both the trial and test functions. Stability of the high-order spectral element method derives from the use of basis functions that are orthogonal with respect to a chosen inner product.

The spectral element bases are derived from a decomposition of the domain into E non-overlapping hexahedral elements, $\Omega = \bigcup_{e=1}^E \Omega^e$, each of which is iso- (or, occasionally, sub-) parametrically mapped from the reference domain $\hat{\Omega} := [-1, 1]^3$ to conform to the geometry of interest. In the reference domain, functions are represented using nodal (Lagrangian) interpolants based upon the Gauss-Lobatto-Legendre (GLL) quadrature points $\xi_i \in [-1, 1]$ (the zeros of $(1-x^2)L'_N(x)$, where $L_N(x)$ is the N th-order Legendre polynomial) [1]. Figure 1 shows a typical toroidal mesh comprising 320 elements of order $N=7$. The use of hex-based elements is critical to the efficiency of the spectral element method as it allows functions to be expressed (locally) in tensor-product form. For example, on Ω^e , one has

$$u(\mathbf{x}(\mathbf{r}))|_{\Omega^e} = \sum_{ijk} u_{ijk}^e h_i(r) h_j(s) h_k(t),$$

where the sum is taken from 0 to N for each index i, j , and k ; \mathbf{x} is the position vector in \mathbb{R}^3 ; \mathbf{r} is the position vector in the reference domain; and u_{ijk}^e is the set of unknown basis coefficients. The Lagrangian basis functions $h_i(r) \in \mathbb{P}_N(r)$ satisfy $h_i(\xi_j) = \delta_{ij}$, $i, j \in \{0, \dots, N\}^2$, where $\mathbb{P}_N(r)$ is the space of polynomials of degree $\leq N$; $\xi_j \in [-1, 1]$ is the j th GLL point associated with $(N+1)$ -point quadrature; and δ_{ij} is the Kronecker delta.

We denote the components of the position vectors as $\mathbf{x} = (x, y, z) = (x_1, x_2, x_3)$ and $\mathbf{r} = (r, s, t) = (r_1, r_2, r_3)$, as needed. (The distinction between the time variable, t , and the third component of the reference coordinate, t , will be clear from the given context.) In the isoparametric formulation, the geometry is represented with the same basis as the solution variables, that is,

$$\mathbf{x}(\mathbf{r})|_{\Omega^e} = \sum_{ijk} \mathbf{x}_{ijk}^e h_i(r) h_j(s) h_k(t).$$

The physical mesh coordinates, \mathbf{x}_{ijk}^e , are generated as part of the preprocessing phase. Typically, the GLL points are distributed along the edges in physical space in an arc-length-preserving fashion and linear (Gordon-Hall) interpolation is used to import the element surface/edge deformation into the element interior. Further details may be found in [2].

3.1. Stiffness Matrix for Anisotropic Diffusion

In the SEM, the stiffness (or coefficient) matrix is never explicitly formed. Rather, since we employ iterative solvers, we simply require the *action* of the stiffness matrix upon a vector, which is effected by evaluating the local matrix-vector products in an element-by-element fashion and assembling the resultant residual vector. To address implementation of the tensor conductivity, we first introduce a few of the components that are central to the SEM matrix-vector multiplication process.

In deformed geometries, extensive use is made of the chain rule to compute the derivatives that appear in the bilinear forms of the weighted residual method. For example, to evaluate the

integrand in the second term of (5), we employ quadrature at the nodal points, which requires evaluation of derivatives of the form

$$\left. \frac{\partial u}{\partial x} \right|_{\mathbf{x}_{mno}^e} = \left(\sum_{j=1}^3 \frac{\partial r_j}{\partial x} \frac{\partial u}{\partial r_j} \right)_{\mathbf{x}_{mno}^e}. \quad (6)$$

Inserting such expansions into (5) and rearranging terms, one derives the local stiffness matrix for the *isotropic* diffusion case, given by

$$A_I^e := \mathbf{D}^T \mathbf{G}^e \mathbf{D} = \begin{pmatrix} D_1 \\ D_2 \\ D_3 \end{pmatrix}^T \begin{pmatrix} G_{11} & G_{12} & G_{13} \\ G_{21} & G_{22} & G_{23} \\ G_{31} & G_{32} & G_{33} \end{pmatrix}^e \begin{pmatrix} D_1 \\ D_2 \\ D_3 \end{pmatrix}. \quad (7)$$

The components of the geometric tensor field, \mathbf{G}^e , are diagonal matrices with entries

$$G_{ij}^e \Big|_{\mathbf{x}_{mno}^e} := \hat{B} J^e \left(\sum_{k=1}^3 \frac{\partial r_i}{\partial x_k} \frac{\partial r_j}{\partial x_k} \right) \Big|_{\mathbf{x}_{mno}^e}, \quad (8)$$

comprising the Jacobian (J^e), local mass matrix (\hat{B}), and metrics ($\frac{\partial r_i}{\partial x_k}$). The product $J^e G_{ij}^e$ is evaluated using point-wise collocation, as is standard with pseudo-spectral methods. The collocation is coupled with point-wise quadrature (i.e., $\hat{B} := \text{diag}(\rho_m \rho_o \rho_n)$, where $\rho_k = \int_{-1}^1 h_k(r) dr$ is the k th GLL quadrature weight), which is viable because the use of GLL nodal bases ensures that the quadrature and approximation errors are of the same order provided that the geometry is sufficiently smooth.

The differentiation matrices in the reference coordinates r_i are $D_1 := (I \otimes I \otimes \hat{D})$, $D_2 := (I \otimes \hat{D} \otimes I)$, $D_3 := (\hat{D} \otimes I \otimes I)$, where \hat{D} is the one-dimensional spectral differentiation matrix

$$\hat{D}_{ij} = \left. \frac{dh_j}{dr} \right|_{\xi_i}, \quad i, j \in [0, \dots, N]^2.$$

The bulk of the computational effort is in applying the derivative operators ($12N^4$ operations per element). These, however, can be cast as *matrix-matrix* products, which are generally fast on vector- and cache-based architectures. The bulk of the memory demand is in accessing the G_{ij}^e s— $6N^3$ entries per element, which is comparable to standard 7-point finite difference methods. Note that if a full mass matrix were used, or if the factored form (7) were not employed, the storage and work would be $O(N^6)$ per element, which would be prohibitive for $N > 5$.

It is straightforward to incorporate a full diffusion tensor, \mathbf{K} , into the framework introduced above. To begin, we expand the second integrand on the left of (5) to obtain

$$\nabla v \cdot \mathbf{K} \cdot \nabla u = \sum_{i,j} \frac{\partial v}{\partial x_i} K_{ij} \frac{\partial u}{\partial x_i} = \sum_{l,m} \sum_{i,j} \frac{\partial v}{\partial r_l} \left(\frac{\partial r_l}{\partial x_i} K_{ij} \frac{\partial r_m}{\partial x_i} \right) \frac{\partial u}{\partial r_m},$$

where the summation indices range from 1 to 3. Inserting the local basis functions and applying quadrature, the local stiffness matrix for a single element Ω^e is $A_{||}^e := \mathbf{D}^T \tilde{\mathbf{G}}^e \mathbf{D}$, where $\tilde{\mathbf{G}}^e := \text{block}(\tilde{G}_{lm}^e)$, with

$$\tilde{G}_{lm}^e = \hat{B} J^e \left(\sum_{i,j} \frac{\partial r_l}{\partial x_i} K_{ij} \frac{\partial r_m}{\partial x_j} \right)_{\mathbf{x}_{mno}^e}.$$

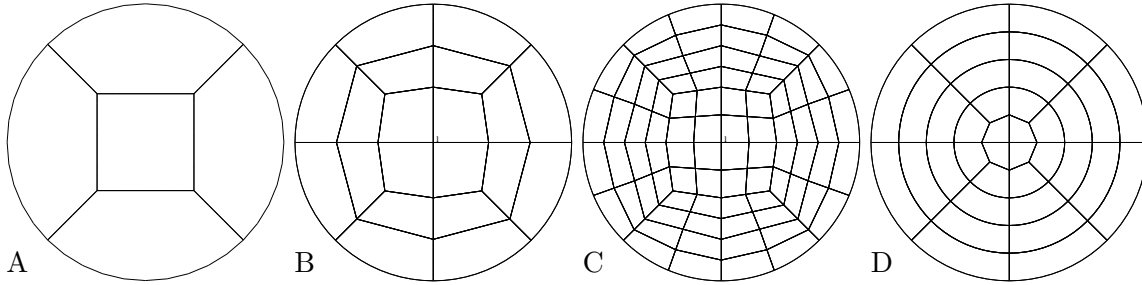


Figure 2. Views of a 5 (A), 20 (B), 80 (C), and 36 (D) spectral element mesh in the torus cross section. Mesh C is obtained as a quad-refine of Mesh B. Mesh A is obtained by coarsening B.

Note that the structure of A_{\parallel}^e is identical to A_I^e ; only the entries in \mathbf{G}^e and $\tilde{\mathbf{G}}^e$ differ. Because the coefficients \tilde{G}_{ij}^e are computed in a preprocessing step, the cost of applying the stiffness matrix in the case of the tensor conductivity is *identical* to the cost of applying the standard SEM stiffness matrix. The action of the global stiffness matrix, which is never formed, is effected by combining the local matrix-vector products with standard finite-element-type assembly and boundary condition application procedures. We refer to [2] for further details.

3.2. Meshing the Toroidal Geometry

We mesh the torus by constructing standard decompositions for cylindrical geometries and then analytically wrapping these into the desired toroidal configuration. This approach can be readily extended to more complex geometries, such as stellarator designs that are being considered for future generation fusion reactors. A typical three-dimensional configuration is illustrated in the isometric and cut-away views of Fig. 1. Four cylindrical cross-sections were considered and are shown in Fig. 2. Mesh C was obtained as a quad-refinement of B, and A was a result of coarsening B. Our preprocessor is based on 32-bit arithmetic and thus generates only seven digits in the input mesh. For some of the more precise computations this had an impact on the final error, so all boundary vertices were first mapped to the unit cylinder prior to applying the toroidal wrap. The solver runs in 64-bit precision so this step eliminated mesh precision as a source of significant error.

4. Steady State Problem

In the following sections, we consider application of the SEM to the model problems described in [6].

To facilitate a detailed survey of the spatial convergence properties, we begin by solving the unperturbed ($\alpha_{mn} \equiv 0$) steady-state problem with $\kappa_I = 1$ and a prescribed source term

$$f = \frac{2\kappa_I}{a^2} (3 - R_0/R), \quad (9)$$

which yields a parabolic profile with $u_{\text{ex}} = 1 - (r/a)^2$.

We consider the mesh cross-sections A, B, and C of Fig. 2 with L layers in the toroidal (ϕ) direction. For each mesh, solutions were computed with $N = 1, 2, \dots, 10$. We also examined 20- and 80-element cross-sections derived directly from successive quad-refinements of Mesh A, that is, cross-sections having square elements in the interior. The results for these, however, were found to be nearly identical to those obtained using Mesh B and C, respectively, and are not presented here.

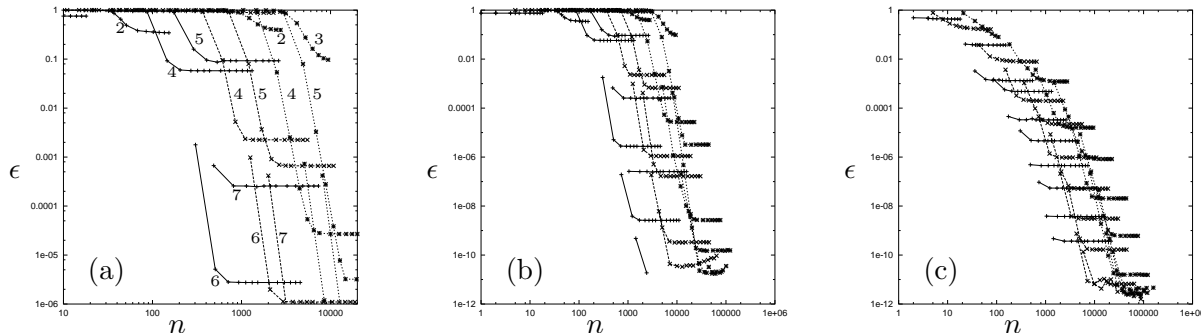


Figure 3. Steady-state L^∞ (pointwise) error vs. number of degrees of freedom for mesh configurations of Fig. 2, A (+), B(\times), and C (*): (a) annotated view indicating polynomial degree N for $\kappa_{\parallel} = 10^8$, (b) full view for $\kappa_{\parallel} = 10^8$ showing range of cases considered, and (c) full view for $\kappa_{\parallel} = 10^0$.

The linear systems were solved using Jacobi-preconditioned conjugate gradient (PCG) iteration with $\underline{u}^0 \equiv 0$ as an initial guess. The iteration was terminated whenever

$$\|\underline{r}^i\|_2 := \|\underline{B}\underline{f} - A\underline{u}^i\|_2 \leq \max(10^{-10}\|\underline{r}^0\|_2, 10^{-11}M_i),$$

where $M_i := \max_{j < i} \|\underline{r}^j\|_2$. The maximum criterion was required to ensure termination in some of the high-anisotropy cases that exhibited an initial steep rise in the PCG residual.

Figure 3 shows the error as a function of the number of degrees of freedom, $n \approx EN^3$, for $\kappa_{\parallel} = 10^k$, with $k=8$ in (a) and (b) and $k=0$ in (c). The error is computed pointwise, $\epsilon := \max_{\mathbf{x}_i \in X} |u(\mathbf{x}_i) - u_{\text{EX}}(\mathbf{x}_i)|$, where X is the set of all nodal points. Each line segment corresponds to the sequence $L=3, 5, 7, 9, 11, 13, 15, 20, 25, 35, 40$, and 45 , for a given mesh, A, B, or C, and value of N . Figure 3 requires some explanation as there are features to note at both the micro and, more importantly, macro scales.

Beginning with the microscale, we see that for a given value of N the error for all three mesh cross-sections is roughly equal when $L=3$. In this case, the error is dominated by the lack of toroidal resolution and the cross-sectional resolution is relatively unimportant. As L increases, the Mesh A error curves level off and saturate at $L \approx 7$; further increases in the toroidal resolution do not result in further error reduction. For sufficiently large N , the error saturates at $L \approx 9$ for Mesh B and at $L \approx 15$ for Mesh C. In general, the error saturates at a lower value of L when N is increased. This trend is to be expected because the toroidal resolution (distance per gridpoint) scales as $(LN)^{-1}$. Once the toroidal geometry is resolved the error is dominated by the discretization error in the cross-section.

The error levels for Mesh A exhibit an even-odd oscillatory behavior that is increasingly pronounced with increasing κ_{\parallel} . For N even, the error is smaller than for $N + 1$. Such even-odd error behavior is common in model problems exhibiting bilateral or equivalent symmetries. We note that the odd-ordered cases for Mesh A are the only ones that do not contain the torus centerpoint. Because the error vanishes at $r = a$, any error at the centerpoint must be associated with a function in the nullspace of A_{\parallel} (i.e., a function with nontrivial radial variation), which is not controlled by a discretization that does not contain the center point.

The more important aspects of Fig. 3 are the macroscopic trends. First, for fixed error, it is always beneficial to increase the approximation order N in favor of refining the mesh (i.e., changing from Mesh A to B to C). This of course is to be expected for problems having smooth solutions, such as considered here. Second, the steepening slopes in Fig. 3(c) give clear evidence

of spectral convergence. On a log-log scale, convergence at any fixed power of n would yield straight lines. The smallest errors achieved are on the order of 10^{-11} , which correlates with the termination criterion of the PCG iteration.

The most striking effect of anisotropy is that the error for the $\kappa_{\parallel} = 10^8$ case is order unity until spectral convergence sets in, at which point the error drops very rapidly, whereas the $\kappa_{\parallel} = 10^0$ case experiences the usual smooth convergence process starting from small n . The dual nature of the anisotropic error behavior results from the requirement that the error in A_{\parallel} (in particular, the radial diffusion) be very small to compensate for the large κ_{\parallel} multiplier. Such stringent error tolerances are most effectively met by high-order methods and the convergence is quite rapid once the essential features of the differential operator are resolved.

5. Evolution of a Gaussian Pulse

We turn now to the unsteady evolution of a Gaussian pulse with initial condition

$$u(0, \mathbf{x}) = e^{-[(R-R_1)^2 - (R_1\phi)^2 - z^2]/\delta^2},$$

where $R_1 = 3.5$, $\delta = 0.1$, $\kappa_{\parallel} = 1$ and $\kappa_I = 0$. With zero diffusivity in the radial direction, energy on any given toroidal surface should be conserved. This is monitored by computing the integral

$$\langle u \rangle(r, t) := \int_0^{2\pi} \int_0^{2\pi} Ru \, d\phi d\theta. \quad (10)$$

Figure 4 shows the ϕ -integrated temperature distribution at different times. There is no visible diffusion in the radial direction despite the fact that the elements are not aligned with thermal isosurfaces. The meshes are based on the cross-section of Fig. 2(b) with 20 elements in the cross-section and 9 elements in the toroidal direction. Polynomial orders of $N = 13$ (389493 dofs) and 15 (599535 dofs) are considered. Timestepping is based on BDF3 with an initial timestep size of 10^{-6} and final step size of 10^{-2} .

Figure 5 (a) shows plots of $\langle u \rangle$ versus r for several time points in the interval $t \in [0, 450]$. Because $\kappa_I = 0$, the energy along any toroidal surface ($r = \text{constant}$) should be conserved and $\langle u \rangle$ should thus be time invariant. Figures 5 (c) and (d) show the departure from the initial condition, $\epsilon(r, t) := |\langle u \rangle(r, t) - \langle u \rangle(r, 0)|$, for several values of t on the same interval. The histories of the mean error, $\epsilon_M := \int \epsilon(r, t) dr$, shown in Fig. 5(b), indicate that the relative error is growing but still $< 2 \times 10^{-5}$ out to time $t = 450$ for $N=13$, while it is relatively flat and well below this level for $N=15$. We remark that the r -integration was done as a post-processing step in 32-bit arithmetic, which is our standard output precision. Thus, 10^{-7} is the best we can expect for this final diagnostic.

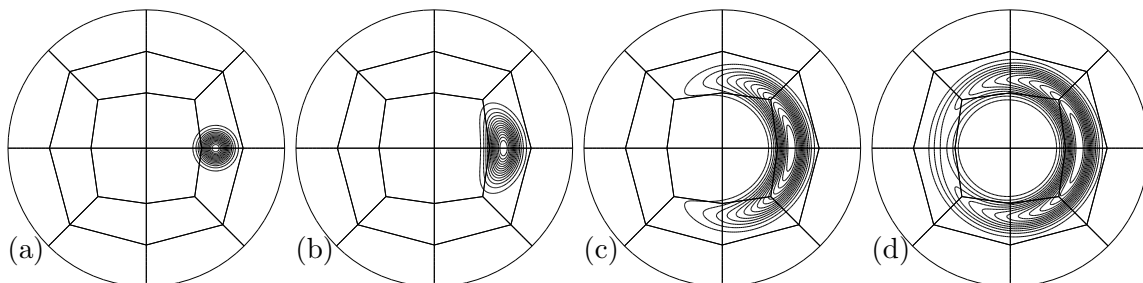


Figure 4. ϕ -integrated temperature distribution for the Gaussian pulse problem using $E = 20 \times 9$ and $N = 15$. Times are $t=0$ (a), 0.493 (b), 6.274 (c), and 17.273 (d).

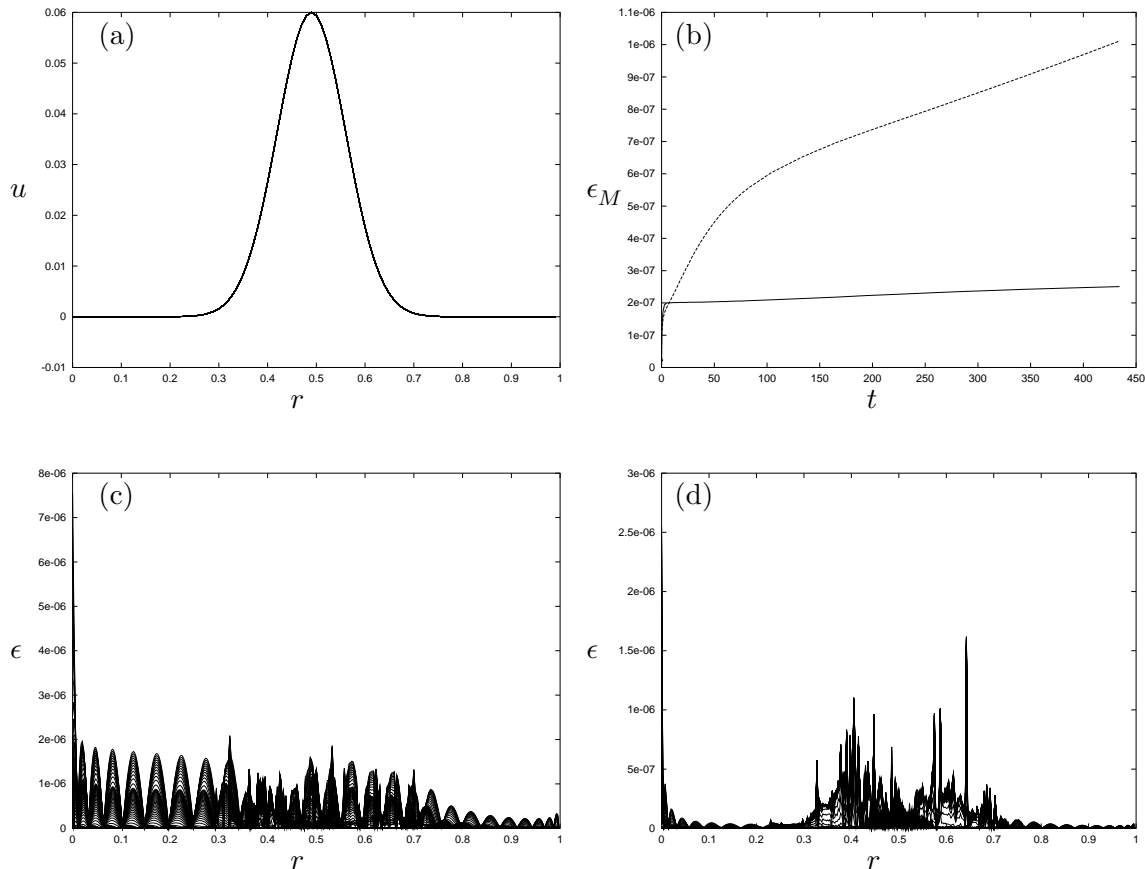


Figure 5. Integrated temperature profiles $\langle u \rangle(r, t)$, (a) and L^2 error history (b) for the for the Gaussian pulse initial condition in the torus computed with an $E = 20 \times 9$ element discretization based on Mesh (b). Polynomial degrees are $N=13$ and 15. The lower figures show the error distribution, $|\langle u \rangle(r, 0) - \langle u \rangle(r, t)|$, for $N=13$ (c) and 15 (d).

6. Tearing Mode Instability

We next consider the perturbation case with α_{mn} in (3) nonzero, which yields magnetic field lines that deviate sinusoidally in ϕ and θ from tangent surfaces of \mathbf{b}_0 . The wave number (m, n) of the perturbation is the same at all radii r . Because of the shear in the magnetic field lines, however, there is potential for a resonant interaction of the perturbation with the base field at the m - n rational surface of \mathbf{b}_0 . This resonance, which has been studied analytically in [3], can lead to a drop in plasma temperature that is potentially detrimental to reactor performance.

We consider the particular case of $(m, n) = (3, 2)$, which corresponds to a rational surface at $r_* \approx .6790229a$. To avoid singularities at $r = 0$ and anomalous diffusion at $r = a$ we set the damping factor in the perturbation \mathbf{b} -field (2) to $g(r) := r^m(a-r)/r_*^{m+1}$. The perturbation in \mathbf{b} leads to the formation of islands of width W that are evident near the 3-2 rational surface in Fig. 6(a), which shows isotherm lines at a toroidal cross-section for the perturbed case. The islands and flattened temperature profiles ($du/dr \rightarrow 0$, Fig. 6(b)) along rays passing through them are manifestations of a local increase in thermal conductivity that can be explained as follows. Because $\kappa_{||}/\kappa_{\perp} \gg 1$, thermal conduction primarily follows the \mathbf{b} -field. Away from the rational surface, the perturbed field lines form wavy sheets and conduction along these field lines stays wrapped on these sheets in a manner similar to the unperturbed case. Conduction across the wavy sheet is possible only through the isotropic (κ_I) component of the conductivity.

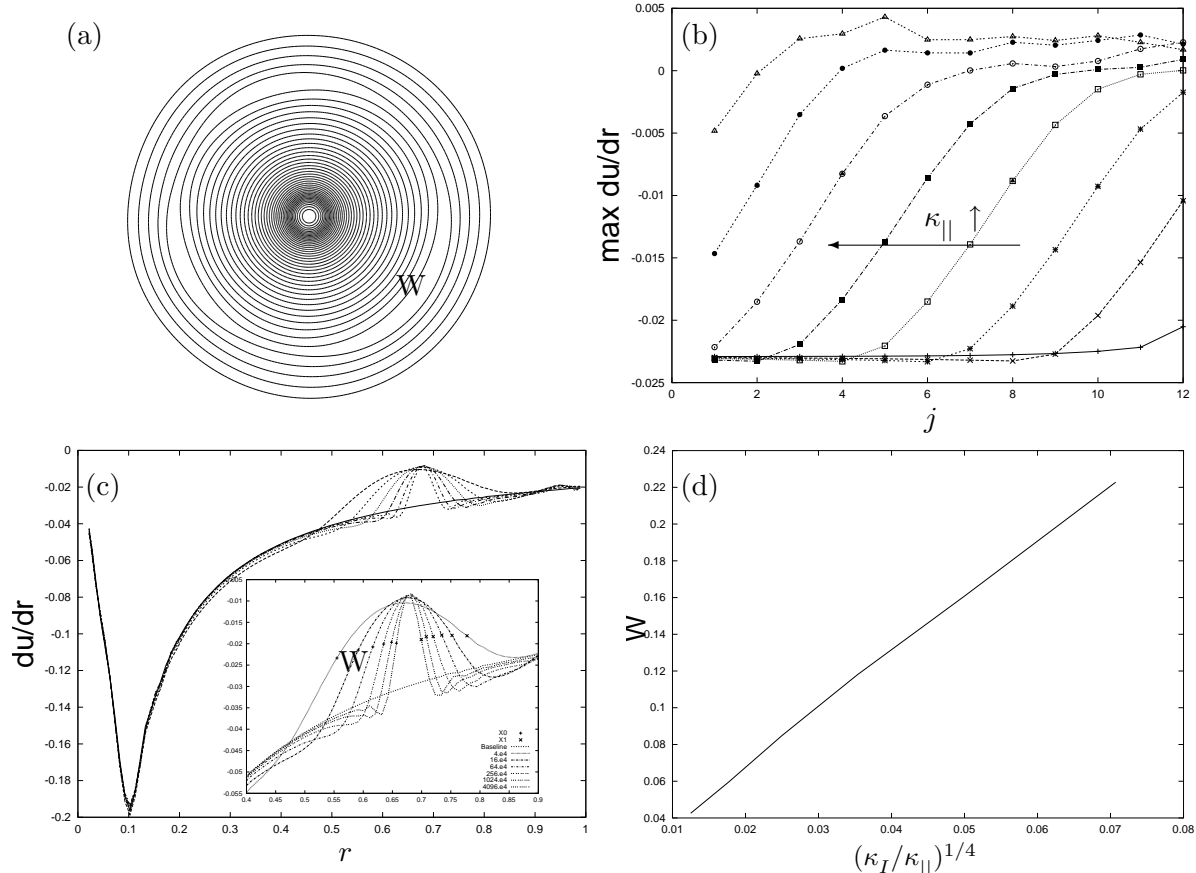


Figure 6. (a) Island formation near the 3–2 rational surface; (b) $\max_r du/dr$ vs. $\alpha_{32} = .00125 \times 2^{j/2}$; (c) du/dr vs. r along a ray passing through the island for the transition cases; and (d) island width vs. $(\kappa_I/\kappa_{\parallel})^{1/4}$ at onset of island formation.

On the rational surface, however, the field lines do not form a proper tangent surface. Here, the perturbation along any given pathline of the base field is constant. Thus, any nontrivial component of the perturbation field is always pointing up or pointing down along any individual (closed) line associated with the base field. (Because the problem is diffusion, the sign of the perturbation vector is immaterial to the end result.) Heat following pathlines initiated on the rational surface does not return to this surface; there is, in effect, a tear in the fabric of the field lines. Aside from the nodal lines ($m\theta - n\phi$ an integer multiple of π), where the amplitude is zero, the tear results in a net conductivity that leads to the flattened profile of Fig. 6.

Detailed asymptotic analysis of the tearing mode presented by Fitzpatrick [3] indicates that the onset of island formation occurs at a critical perturbation amplitude $\alpha_{32} = \alpha_c \sim (\kappa_I/\kappa_{\parallel})^{1/2}$ and that the island width *at onset* scales as $W \sim (\kappa_I/\kappa_{\parallel})^{1/4}$. Fig. 6(b) shows curves of $\max du/dr$ for several values of $\kappa_I/\kappa_{\parallel}$, where du/dr is taken along a ray emanating from $r = 0$ through an island. Moving from left to right, the values of $\kappa_I/\kappa_{\parallel}$ increase by a factor of 4, starting with $\kappa_I/\kappa_{\parallel} = 6.10352 \times 10^{-9}$. Each curve is parameterized by $\alpha_{32} = .00125 \times 2^{j/2}$. At the mid-values of the curves ($du/dr \approx -.01$), which indicate the onset of profile flattening, the spacing is $\Delta j = 2$. Thus, a four-fold increase in $\kappa_I/\kappa_{\parallel}$ is accompanied by a two-fold increase in α_c , in accord with the asymptotic theory.

We estimate the island width at transition by examining the profiles for the cases where

$\alpha_{32} = \alpha_c(\kappa_I/\kappa_{||})$ (i.e., $du/dr \approx -.01$). Plots of du/dr are shown in Fig. 6(c). The hump in these curves, corresponding to $du/dr \rightarrow 0$, indicates the presence of an island. The island width was estimated by finding the two crosspoints where each curve assumes a value half-way between its peak and an $\alpha_{32} = 0$ baseline curve (Fig. 6(c), inset). The associated widths are plotted in Fig. 6(d) versus $(\kappa_I/\kappa_{||})^{1/4}$. The straight line behavior shows clear agreement with the asymptotic theory [3].

7. Discussion and Conclusions

We have presented a spectral element method for solution of highly anisotropic diffusion in toroidal domains, which is a central problem in predictive fusion simulation. Computing the diffusive transport on the base field (\mathbf{b}_0) is relatively straightforward and the SEM does not require field-fitted grids. When the perturbation field is present, however, the problem is significantly more challenging, particularly for $\kappa_{||}/\kappa_I > 10^6$. First, the condition number of the system scales directly as $\kappa_{||}/\kappa_I$, implying high costs for Jacobi preconditioned conjugate gradients. Clearly, some type of multilevel preconditioner is desirable. Such an approach, however, will have to reflect the intrinsic anisotropy of the originating operator. Second, we remark that the results of Section 6 were computed using Mesh D of Fig. 2, which has elements that conform to the \mathbf{b}_0 field lines at the outer values of r . This choice was originally motivated by the perceived difficulty of the problem. However, our initial attempts to recreate the results of Fig. 6 using meshes *A*, *B*, or *C* have been unsuccessful. In particular, we are not able to correctly predict the transition observed in the high $\kappa_{||}$ cases (the leftmost curves in Fig. 6(b)). We are currently investigating if the difficulty stems from quadrature error associated with spatial variations in $\kappa_{||}$ or if it is due to another source. Despite these challenges, it is clear that high-order methods offer significant potential for accurate prediction of challenging physics such as encountered in fusion development.

Acknowledgments

This work was supported by the Mathematical, Information, and Computational Sciences Division subprogram of the Office of Advanced Scientific Computing Research, U.S. Department of Energy, under Contract W-31-109-Eng-38. I thank Steve Jardin at Princeton Plasma Physics Laboratory for many useful discussions on this topic.

- [1] Canuto C, Hussaini Y, Quarteroni A, and Zang T 1986 (Springer-Verlag)
- [2] Deville M, Fischer P, Mund E 2002 (Cambridge University Press)
- [3] Fitzpatrick R 1995 *Phys. Plasmas* **2** 826
- [4] Glasser A H and Tang X Z 2004 *Comp. Phys. Comm.* **164** 237
- [5] Jardin S C 2004 *J. Comp. Phys.* **200** 133
- [6] URL: <http://w3.pppl.gov/cemm/project.html>